Electronic and valley properties of Janus Te*M*Si*X*$_2$ (M = Mo, W; X = P, As) monolayers and Te*M*Si*X*$_2$/CrI$_3$ heterostructures

Yang Yang [1,2] Tao Li,[1,2] Shi-quan Feng,[1,2] and Hong-Yan Lu[3]

[1]*School of Electronics and Information, Zhengzhou University of Light Industry, Zhengzhou 450002, China*
[2]*Henan Key Laboratory of Magnetoelectronic Information Functional Materials,*
Zhengzhou University of Light Industry, Zhengzhou 450002, China
[3]*School of Physics and Physical Engineering, Qufu Normal University, Qufu 273165, China*

In this study, we investigate Te*M*Si*X*$_2$ (M = Mo and W; X = P and As) Janus monolayers, identifying them as direct band-gap semiconductors exhibiting two distinctive valley within both the conduction and valence bands. Te*M*Si*X*$_2$ exhibits significant valley spin splitting (VSS) in the valence band, especially in TeWSiP$_2$ and TeWSiAs$_2$ (up to 0.48 and 0.53 eV). Furthermore, the construction of Te*M*Si*X*$_2$/CrI$_3$ heterostructure introduces valley polarization, with magnitudes ranging from 2.9 meV for TeMoSiP$_2$/CrI$_3$ to up to 26.1 meV for TeWSiAs$_2$/CrI$_3$. Manipulating the magnetization direction of CrI$_3$ or the interlayer spacing results in alterations of valley polarization in Te*M*Si*X*$_2$/CrI$_3$. These findings provide valuable guidance for the further development of valleytronic devices based on Te*M*Si*X*$_2$ Janus monolayers.

I. INTRODUCTION

In recent years, significant progress has been made in the realm of two-dimensional (2D) materials, fueling an in-depth investigation into their unique characteristics and potential applications in various fields [1,2]. This progress has brought to light a notable discovery in valleytronics research, specifically in the manipulation of the valley degree of freedom within 2D materials [3–9]. The valley degree of freedom, encompassing the energy extrema within the electronic-band structure, plays a crucial role in facilitating the selective excitation or manipulation of electrons. These distinct valleys, located at the K and K' points of the hexagonal Brillouin zone, demonstrate robustness derived from their significant separation in momentum space, enabling them to withstand low-energy phonons and scattering from nonmagnetic impurities. The strategic application of this valley degree of freedom in 2D materials, such as transition-metal dichalcogenides (TMDs) [10,11], introduces innovative pathways for information processing and storage, thereby positioning 2D valleytronic materials as a promising platform for advancing high-performance quantum devices.

The fabrication of Janus monolayers in TMDs, exemplified by MoSSe, opens up additional avenues for advancing valleytronics. Achieved by harnessing the hexagonal structure of TMDs, the unique architecture of Janus monolayers could serve as the foundation for amalgamating the desirable properties of TMDs with remarkable characteristics, as evidenced by phenomena such as the Rashba splitting and out-of-plane piezoelectric polarization [12]. Additionally, Janus monolayers present a distinctive vertical asymmetric configuration, arising from the noticeable difference in atoms on each side of the structure. This asymmetry results in entirely distinct physical and chemical properties on each side [13–15]. In the case of MoSSe, the combination of inversion symmetry

breaking and strong spin-orbit coupling (SOC) yields a remarkable multivalleyed band structure and a robust interplay between spin and valley physics [16].

Despite substantial research efforts to achieve Janus monolayers based on TMDs, there is still a robust demand for innovative 2D Janus materials that demonstrate superior performance. Janus configurations within the MA_2Z_4 family are anticipated to emerge as promising materials in this context [17]. Until now, numerous research groups have dedicated their investigations to exploring Janus configurations of MA_2Z_4 monolayers, aiming to manipulate their physical properties and broaden their applications [18–21]. For example, Yu *et al.* predicted that MSiGeN$_4$ (M = Mo and W), a Janus form of the MA_2Z_4 family achieved by substituting one Si-N bond with a Ge-N bond, exhibits characteristics of an indirect band-gap semiconductor with appropriate band-edge energy levels [20]. Moreover, it exhibits high optical absorption in the visible spectrum and a notable difference in electron-hole mobility. These unique properties position MSiGeN$_4$ as a highly efficient photocatalyst for the comprehensive water-splitting process. Rezavand *et al.* explored Janus Te*M*Si*X*$_2$ (M = Mo, W; X = N, P, As) monolayers and observed Rashba spin-splitting in valence and conduction bands, accompanied by a Mexican hat dispersion in the topmost valence band. These distinctive properties position Janus Te*M*Si*X*$_2$ as a promising material for future spintronic devices [21].

Here, we comprehensively investigate Te*M*Si*X*$_2$ (M = Mo and W, X = P and As) Janus monolayers, focusing on analyzing their electronic and valleytronic properties. These monolayers demonstrate properties typical of direct band-gap semiconductors, featuring two distinct valleys in both the conduction and valence bands. Te*M*Si*X*$_2$ displays significant valley spin splitting (VSS) in the valence band and minimal splitting in the conduction band. Specifically, TeWSiP$_2$

and TeWSiAs$_2$ manifest notably high values of VSS, reaching up to 0.48 and 0.53 eV, respectively. Stacking CrI$_3$ on TeMSiX_2 to form a TeMSiX_2/CrI$_3$ heterostructure induces valley polarization in both band edges of TeMSiX_2. Specifically, the valley polarization of TeMoSiP$_2$/CrI$_3$ exhibits approximately 2.9 meV, while TeWSiAs$_2$/CrI$_3$ demonstrates a polarization of up to 26.1 meV. Furthermore, by manipulating the magnetization direction of the CrI$_3$ monolayer or adjusting the interlayer spacing between TeMSiX_2 and CrI$_3$, we can effectively modulate the valley polarization within the TeMSiX_2/CrI$_3$ heterostructure. These insights provide valuable guidance for the future development of valleytronic devices based on TeMSiX_2 Janus monolayers.

II. COMPUTATIONAL DETAILS

This study employs density-functional theory (DFT) first-principles electronic calculations with the Vienna *ab initio* simulation package (VASP) code [22]. Exchange-correlation interactions are described using the Perdew-Burke-Ernzerhof (PBE) functional within the generalized gradient approximation (GGA) [23,24]. Upon convergence testing, a kinetic energy cutoff of 500 eV is selected, and a $12 \times 12 \times 1$ Gamma-pack k-point mesh is utilized for Brillouin zone integration. A 20 Å vacuum layer along the z direction is added to avoid periodic boundary condition effects. For accurate band structures of monolayers, the Heyd-Scuseria-Ernzerhof (HSE06) hybrid functional is adopted [25]. Additionally, detailed calculations using both standard PBE-GGA and the GGA+U methods for TeMSiX_2 monolayers are also performed [26]. The phonon spectrum is computed using the PHONOPY code over a $3 \times 3 \times 1$ supercell [27]. Moreover, *ab initio* molecular dynamics (AIMD) simulations are conducted at 500 K for a total duration of 6 ps [28]. The DFT-D3 method is applied for van der Waals (vdW) correction in heterostructures [29], and the GGA + U method addresses strong correlation effects of the 3d electrons of Cr atoms, with U set to 2.7 eV and exchange interaction J set to 0.7 eV [30,31]. During the structure optimization, the in-plane structure parameters and atom positions are fully relaxed until the force is less than 0.01 eV/Å.

To further elucidate the valley properties, we calculate the Berry curvature $\Omega(\mathbf{k})$ using the standard linear response Kubo formula [32,33]

$$\Omega(\mathbf{k}) = -\sum_n 2f_n Im \sum_{n \neq n'} \frac{\langle \psi_{n\mathbf{k}}|\mathbf{v}_x|\psi_{n'\mathbf{k}}\rangle \langle \psi_{n'\mathbf{k}}|\mathbf{v}_y|\psi_{n\mathbf{k}}\rangle}{(E_{n\mathbf{k}} - E_{n'\mathbf{k}})^2}, \quad (1)$$

where f_n is the Fermi-Dirac distribution function, $\mathbf{v}_{x,y}$ represent the velocity operators, and $|\psi_{n\mathbf{k}}\rangle$ denotes the Bloch function with the eigenvalue $E_{n\mathbf{k}}$ of the Fourier-transformed Wannier Hamiltonian. The Fourier-transformed Wannier Hamiltonian is determined by projecting the DFT Hamiltonian onto a Wannier basis using the WANNIER90 package [34,35].

III. RESULTS AND DISCUSSION

As depicted in Fig. 1, the TeMSiX_2 monolayers manifest a heightened degree of asymmetry when compared to TMDs. The formation of these unique monolayers
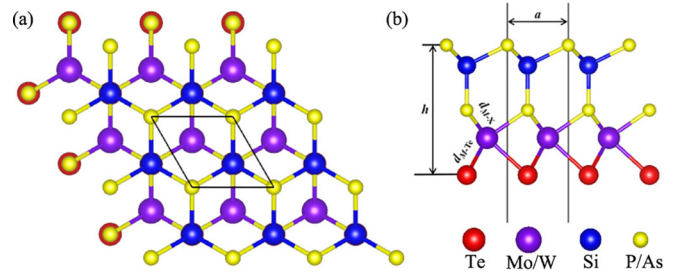

FIG. 1. Crystal structures of TeMSiX_2 (M = Mo, W; X = P, As) monolayers from the side (a) and top (b) views, where the black solid lines denote the primitive cell.

involves selectively removing SiP/SiAs atoms from one side of MoSi$_2$P$_4$/MoSi$_2$As$_4$ and substituting the remaining P/As atoms with Te on that same side. This specific arrangement gives rise to asymmetry, wherein the atomic plane containing transition-metal atoms lacks mirror symmetry. Hence, the TeMSiX_2 monolayers incorporate features originating from 2D materials found in both the TMDs and the MA$_2$Z$_4$ family.

After relaxation, the optimized structural parameters are detailed in Table I. As expected, an expansion in lattice constant occurs in structures with larger atomic numbers, transitioning from P to As. Specifically, for TeMoSiP$_2$ and TeWSiAs$_2$, the lattice constants are determined to be 3.493 Å and 3.609 Å, respectively. Additionally, Janus TeMSiX_2 monolayers exhibit minimal changes in M-Te bond lengths (d_{M-Te}), while notable variations in d_{M-X} are directly influenced by the atomic radius difference between P and As.

The structural stability of TeMSiX_2 monolayers is assessed through various methods. The elastic moduli, obtained using the energy-vs-strain approach, are listed in Table I. These values adhere to the Born-Huang criteria ($C_{11} > 0$, $C_{11} > |C_{12}|$), demonstrating the robust mechanical stability of TeMSiX_2 monolayers. Furthermore, phonon spectra and AIMD simulations are conducted to evaluate dynamical and thermal stability, as detailed in the Supplemental Material [26]. Consequently, the mechanical, dynamic, and thermal stability of TeMSiX_2 monolayers suggests their potential for experimental exploration, akin to MoSi$_2$N$_4$. Previous studies on TeMSiX_2 monolayers also endorse this assertion [19,21].

Our attention now turns to the electronic structures of TeMSiX_2 monolayers, which are given in Figs. 2 and 3. TeMoSiP$_2$ is chosen for illustrative purposes due to the comparable properties among these four materials. Illustrated in Fig. 2(a) is the orbital-resolved band structure of the TeMoSiP$_2$ monolayer, where the effect of SOC is not taken into account. Evidently, the TeMoSiP$_2$ monolayer presents itself as a direct band-gap semiconductor with a band gap of 1.39 eV located at the K/K' point, highlighting its potential application in optoelectronics. Remarkably, both the valence and conduction bands in TeMoSiP$_2$ monolayers feature two energy-degenerate valleys located at the K and K' points. The valence-band maximum (VBM) is primarily attributed to the Mo-$d_{xy}/d_{x^2-y^2}$ orbitals, while the conduction-band minimum (CBM) is mainly influenced by the d_{z^2} orbital. Additionally, electronic states at the Fermi level of -0.7 eV are predominantly governed by the p orbitals of Te or As.

TABLE I. Comparison of four TeMSiX_2 monolayers, including the optimized lattice constant (a), the atomic layer thickness (h), the nearest bond lengths of M-Te ($d_{M-\text{Te}}$) and $M - X$ (d_{M-X}), the elastic moduli (C_{11} and C_{12}), the band gaps without (E_g) and with SOC (E'_g) obtained using HSE functional, the VSS value (Δ_{VSS}), and the values of Berry curvature [$\Omega(\text{K})$].

	a (Å)	h (Å)	$d_{M-\text{Te}}$ (Å)	d_{M-X} (Å)	C_{11} (N/m)	C_{12} (N/m)	E_g (eV)	E'_g (eV)	Δ_{VSS} (eV)	$\Omega(\text{K})$ (Bohr^2)
TeMoSiP$_2$	3.493	6.492	2.742	2.447	152.13	35.84	1.39	1.27	0.20	108.1
TeMoSiAs$_2$	3.601	6.776	2.754	2.554	132.28	35.22	1.16	1.03	0.22	134.1
TeWSiP$_2$	3.501	6.490	2.748	2.449	157.06	32.66	1.28	1.00	0.48	186.9
TeWSiAs$_2$	3.609	6.773	2.759	2.556	136.22	32.45	1.05	0.73	0.53	325.3

Upon activation of the SOC effect, illustrated in Fig. 2(b), the spin degeneracy undergoes lifting, causing a reduction in the band gap from 1.39 to 1.27 eV. Noteworthy is the substantial VSS ($\sim$0.20 eV) observed at the VBM, originating from the SOC effect. The value of VSS (Δ_{VSS}) is comparable to that observed in monolayer MoS$_2$ (0.15 eV) and MoSSe (0.17 eV) [5,16]. In TeWSiP$_2$ and TeWSiAs$_2$ monolayers, Δ_{VSS} can reach up to 0.48 and 0.53 eV, respectively. This significant VSS results from the pronounced SOC effect of the W atom. Time-reversal symmetry plays a pivotal role in determining the behavior of spin splittings at the K and K' valleys, establishing an interplay between spin and valley physics. The VSS at K and K' points exhibit opposite signs, while their absolute magnitudes remain identical, as illustrated in Figs. 2(b), 2(d) and 3(b), 3(d). The opposite sign of the spin-splitting bands arises from the combined effects of inversion symmetry breaking and SOC. Moreover, the maintenance of energy degeneracy across distinct spin channels for both valleys is a direct consequence of time-reversal

symmetry [$E_\uparrow(k) = E_\downarrow(-k)$]. Such remarkable VSS in TeMSiX_2 monolayers can be further quantified experimentally through techniques such as absorption spectroscopy [36,37], making them promising candidates for applications in the realm of valleytronics.

In contrast to the valence band, the conduction band edges show a minimal Δ_{VSS} ($\sim$33 meV) due to distinct dominant orbitals. Considering SOC and approximating it as an intra-atomic contribution with the leading-order term, the SOC term in the Hamiltonian is $\hat{H}'_{SOC} \approx -\frac{\lambda\tau}{2}(\hat{\sigma}_z - 1)\hat{s}_z$, where $\hat{s}_z$ is the spin Pauli matrix, λ is the effective SOC strength, $\tau = \pm 1$ is the valley index (K/K'), and σ_z denotes Pauli matrices for the two basis functions [5]. This implies that VSS results from an asymmetric potential gradient in the in-plane direction. Thus the in-plane $d_{x^2-y^2}/d_{xy}$ orbitals, with strong SOC, contribute significantly to VSS in the valence band, while the out-of-plane d_{z^2} orbital results in minimal effects on VSS in the conduction band.
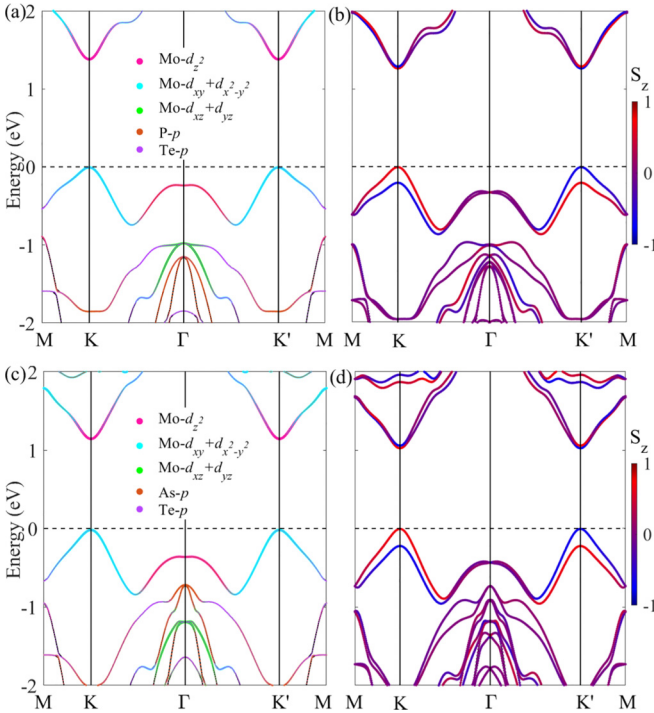

FIG. 2. (a) Orbital-resolved and (b) Spin-projected band structures for TeMoSiP$_2$ within HSE. (c) Orbital-resolved and (d) Spin-projected band structures for TeMoSiAs$_2$ within HSE.
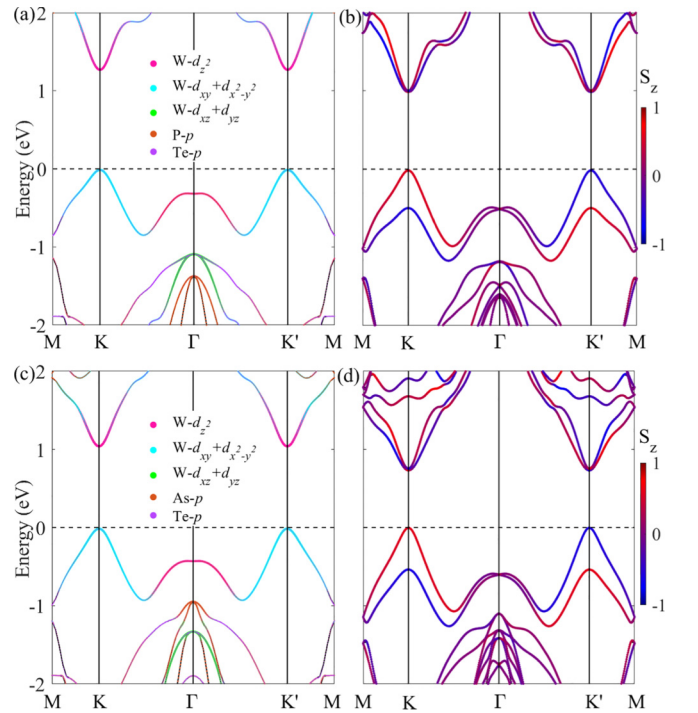
FIG. 3. (a) Orbital-resolved and (b) spin-projected band structures for TeWSiP$_2$ within HSE. (c) Orbital-resolved and (d) spin-projected band structures for TeWSiAs$_2$ within HSE.
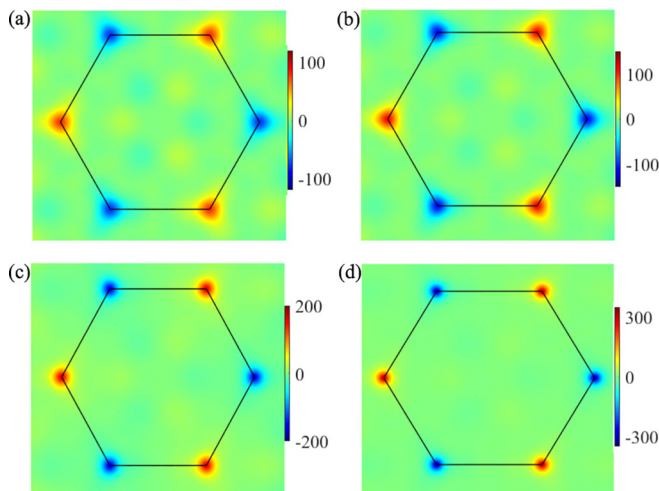
FIG. 4. Contour maps of the Berry curvature for $TeMoSiP_2$ (a), $TeMoSiAs_2$ (b), $TeWSiP_2$ (c), and $TeWSiAs_2$ (d).

The Berry curvatures over the 2D Brillouin zone for four monolayers are depicted in Fig. 4, derived using Eq. (1). Notably, the Berry curvatures at the K and K' valleys are considerable, sharing identical absolute values but displaying opposite signs, thereby indicating the presence of valley-contrasting Berry curvatures in $TeMSiX_2$. The magnitudes of the Berry curvature at the K point are detailed in Table I, revealing that $TeWSiAs_2$ exhibits the highest value at 325.3 $Bohr^2$. This substantial value is attributed to the influence of significant VSS in $TeWSiAs_2$.

These valley-contrasting Berry curvatures enable the valley Hall effect in $TeMSiX_2$ under an in-plane electric field [38]. As shown in Fig. 5(a), moderate hole doping will cause holes originating from the $K(K')$ valley to accumulate at the left (right) edge, realizing the valley Hall effect. Furthermore, the valley Hall effect can also be realized under optical illumination, as depicted in Fig. 5(b). Linearly polarized light excites spin-up holes and spin-down electrons at K, while spin-down holes and spin-up electrons at K'. With the application of an in-plane electric field, spin-up holes (electrons) from the K (K') valley migrate to the left boundary, while spin-down electrons (holes) from the K (K') valley accumulate at the right boundary, achieving the valley Hall effect in $TeMSiX_2$ monolayers.
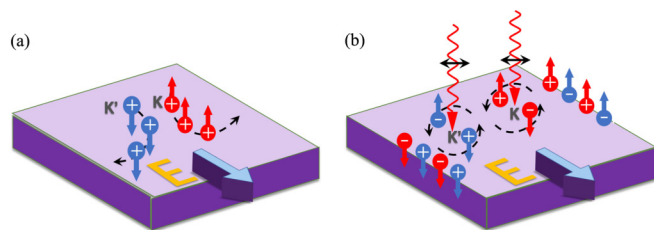

FIG. 5. (a) Diagram of the spin and valley Hall effects in hole-doped $TeMSiX_2$ monolayers. (b) Diagram of the spin and valley Hall effects in $TeMSiX_2$ monolayers under linearly polarized light. In (a) and (b), red/blue balls indicate the carriers from the K/K' valleys, $\pm$ symbols in the balls indicate holes/electrons, and up/down arrows in indicate the spin-up/spin-down.
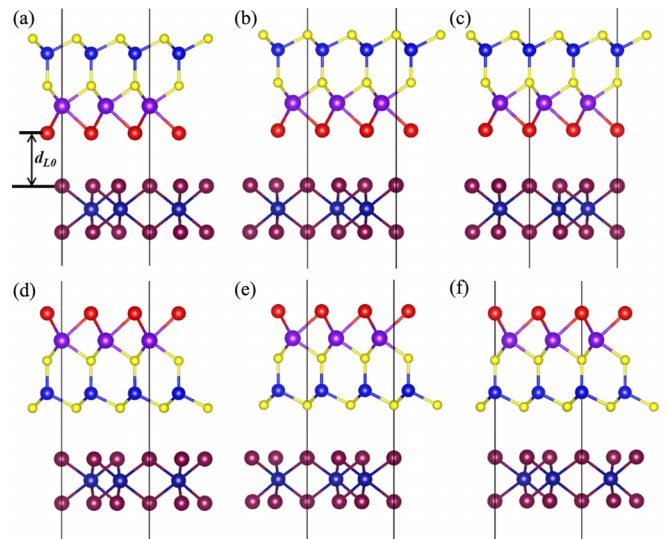

FIG. 6. Side views of $TeMSiX_2/CrI_3$ in six stacking arrangements: C-1 to C-6 (a)–(f).

$TeMSiX_2$ monolayers, with energetically degenerate valleys in their band edges, emerge as promising valleytronic materials. However, efficiently harnessing the valley degree of freedom requires strategic valley polarization generation. We propose constructing a $TeMSiX_2/CrI_3$ heterostructure with a ferromagnetic substrate, inspired by the successful valley splitting in WSe_2/CrI_3 [39–42]. A 2×2 supercell of $TeMSiX_2$ is utilized to match the unit cell of CrI_3. As established in prior research, the WSe_2/CrI_3 heterostructure displays three distinct stacking orders [42]. However, in $TeMSiX_2$ monolayers, the presence of diverse atoms on the two sides leads to a twofold increase in the potential number of stacking arrangements. The crystal structures of the heterostructures are illustrated in Fig. 6 for comparative analysis. Within configuration C-1, a Te/Si atom is positioned directly above a Cr atom. Configuration C-2 features a Mo atom directly above a Cr atom, while in C-3, a P atom in the top layer aligns directly with a Cr atom. The stacking arrangement of C-4 to C-6 can be viewed as the reverse counterpart of C-1 to C-3, involving the exchange of the two sides of the $TeMSiX_2$ monolayers.

The binding energies for the six stacking configurations are determined through the formula

$$E_b = (E_{hete} - E_{CrI_3} - E_{TeMSiX_2})/N, \qquad (2)$$

where E_{hete}, E_{CrI_3}, and E_{TeMSiX_2} represent the total energies of the $TeMSiX_2/CrI_3$ heterostructure, CrI_3 monolayer, and $TeMSiX_2$ monolayer, respectively. The symbol N signifies the total number of atoms. For all $TeMSiX_2/CrI_3$ heterostructures, the C-1 stacking configuration consistently emerges as the most stable. Specifically, in the case of $TeMoSiP_2/CrI_3$, upon reaching structural equilibrium, Table II outlines the lattice constant and binding energies for various stacking arrangements, with C-1 $TeMoSiP_2/CrI_3$ exhibiting a calculated binding energy of -28.1 meV/atom. This strength is comparable to that of other van der Waals heterostructures reported, such as $MoSi_2N_4/CrCl_3$ and GeP/graphene heterostructures [43,44], suggesting the potential experimental realization of $TeMoSiP_2/CrI_3$ heterostructure.

TABLE II. Comparison between three stackings of TeMoSiP$_2$/CrI$_3$. The a denotes the optimized lattice constant and d_{L0} the equilibrium interlayer spacing. The E$_b$ represents the binding energy per atom. $E_{\sigma+}$ and $E_{\sigma-}$ denote the transition energies for right-handed (σ^+) and left-handed (σ^-) circular polarizations, respectively, while ΔE_σ represents the valley polarization.

Stacking	a (Å)	d_{L0} (Å)	E$_b$ (meV)	$E_{\sigma+}$ (meV)	$E_{\sigma-}$ (meV)	ΔE_σ (meV)
C-1	6.944	3.628	−28.1	955.5	952.6	2.9
C-2	6.944	3.642	−27.4	958.4	946.7	11.7
C-3	6.938	3.817	−24.8	963.6	961.4	2.2
C-4	6.942	3.538	−23.6	957.0	956.6	0.4
C-5	6.938	3.756	−21.0	965.6	965.3	0.3
C-6	6.939	3.519	17.1	963.1	944.0	19.1

Table II reveals that the C-1 to C-3 stacking configurations exhibit a minimal energy barrier, as evidenced by their comparable binding energies (E$_b$). However, C-4 to C-6, where the P atom in the bottom layer couples with CrI$_3$, consistently demonstrates higher binding energies. For the C-1 stacking arrangement, the lattice constant is 6.944 Å, closely aligning with experimental and theoretical results for the bare CrI$_3$ monolayer [45,46], resulting in a slight interface mismatch. Simultaneously, the interlayer distance (d_{L0}) measures 3.628 Å, exceeding that of the MoSi$_2$N$_4$/CrCl$_3$ heterostructure but resembling the WSe$_2$/CrI$_3$ case [43,46]. Additionally, the physical binding of monolayer TeMoSiP$_2$ to CrI$_3$ does not impact its magnetic properties, with the CrI$_3$ layer maintaining ferromagnetism. The magnetic moment remains at 3.2 μ_B on each Cr atom and 6.0 μ_B for one CrI$_3$ unit cell, equivalent to its states in bare CrI$_3$.

Although there are minor structural differences, the band structures obtained for the six stacking arrangements, exemplified by the C-1 configuration depicted in Fig. 7(a), demonstrate significant similarity. The heterostructure itself manifests a global band gap of 0.2 eV, contrasting with the individual band gaps of 0.75 eV for bare CrI$_3$ and 1.02 eV for TeMoSiP$_2$ obtained by GGA method. In the energy range from −1.0 to +1.5 eV, the orbital hybridization between CrI$_3$ and TeMoSiP$_2$ is notably weak. Notably, the bands projected onto the Mo atom near both the VBM and CBM of the TeMoSiP$_2$ layer closely resemble those of the free-standing TeMoSiP$_2$, indicating the well-preserved nature of both K and K' valleys. Evidence for this preservation can also be observed in the spin-projected band structures depicted in Fig. 7(b). The magnetic proximity effect (MPE) induced by CrI$_3$ breaks the time-reversal symmetry, resulting in the lifting of energy degeneracy between the two valleys, expressed as $[E_\uparrow(k) \neq E_\downarrow(-k)]$. The valley polarization ΔE_σ, defined as the difference between $E_{\sigma+}$ and $E_{\sigma-}$, is visually apparent in Fig. 7(c). Here, $E_{\sigma+}$ and $E_{\sigma-}$ represent the transition energies for the optical pumping with right-handed (σ^+) and left-handed (σ^-) circular polarizations, respectively. Interestingly, the obtained ΔE_σ for TeMoSiP$_2$/CrI$_3$ is 2.9 meV, corresponding to effective magnetic fields of about 14–29 T, respectively, based on the reported value of 0.1–0.2 meV/T in a few experiments [47–51]. This polarization energy is
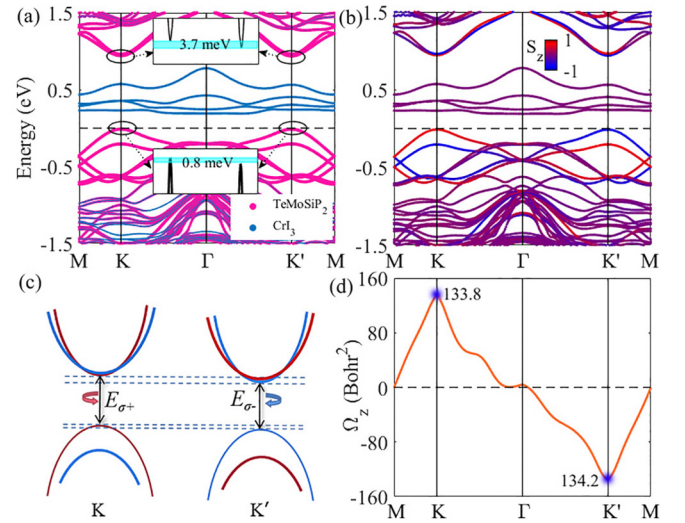

FIG. 7. (a) Atom-projected band structures of the C-1 stacking TeMoSiP$_2$/CrI$_3$ heterostructure, with an inset providing a zoomed view of the valley polarization in both conduction and valence bands. (b) Spin-projected band structures of the C-1 stacking heterostructure, with up- and down-spin bands indicated by red and blue colors, respectively. (c) Pictorial representation highlighting features at the K and K' valleys, where $E_{\sigma+}$ and $E_{\sigma-}$ represent the transition energies for the optical pumping with right-handed (σ^+) and left-handed (σ^-) circular polarizations, respectively. (d) Berry curvature of C-1 stacking TeMoSiP$_2$/CrI$_3$ along the high-symmetry points path.

4.2, 4.4, and 26.1 meV for TeMoSiAs$_2$/CrI$_3$, TeWSiP$_2$/CrI$_3$, and TeWSiAs$_2$/CrI$_3$, respectively [26]. The achievement of valley polarization within the TeMSiX_2/CrI$_3$ heterostructure suggests broader potential for applications in valleytronics.

The lifted valley degeneracy persists across various stacking configurations or distinct TeMSiX_2 on CrI$_3$, indicating the robustness of MPE valley polarization. Additionally, as indicated in Table II, the substantial valley polarization in the C-2 stacking patterns suggests that stacking configurations could amplify the magnitude of the valley Zeeman effect, providing a means to manipulate the valley pseudospin. The proposed TeMoSiP$_2$/CrI$_3$ heterostructure, akin to free-standing TeMoSiP$_2$, lacks inversion symmetry, resulting in a nonvanishing Berry curvature. In Fig. 7(d), the out-of-plane Berry curvature $\Omega(k)$ displays two peaks at K and K' with opposite signs, with a maximum value of 133.8 Bohr^2 at K points, slightly differing from the observed value of −134.2 Bohr^2 at K' points. This nonzero Berry curvature corresponds to an anomalous Hall effect arising from the coexistence of SOC and magnetism, signifying an anomalous Hall effect due to the simultaneous presence of SOC and magnetism.

Our investigation also extends to examining how magnetization direction and interlayer spacing affect valleytronic and electronic properties. The trends among the four compounds exhibit a notable similarity, and TeMoSiAs$_2$/CrI$_3$ is selected for illustration due to its clear band separation and substantial valley polarization. By adjusting the external magnetic-field direction, the magnetization of the CrI$_3$ substrate can be experimentally controlled. As depicted in Fig. 8(a), transitioning from out-of-plane to in-plane magnetization results in a change in the magnetization angle θ (along z axis) from 0 to
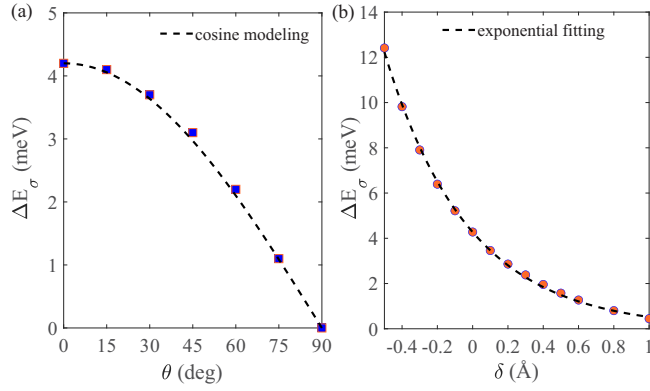
FIG. 8. Calculated valley polarization ΔE_σ of TeMoSiAs$_2$/CrI$_3$, depicted as a function of (a) the magnetization direction of CrI$_3$ and (b) the interlayer distance deviation from the equilibrium state.

$90°$. This alteration gives rise to a cosine function relationship in the valley polarization ΔE_σ:

$$\Delta E_\sigma^\theta = \Delta E_\sigma \cos\theta. \tag{3}$$

Additionally, in experimental scenarios, researchers can manipulate the valley degrees of freedom by adjusting the magnitude of an external magnetic field [49,50]. To emulate this impact, we modify the interlayer distance within the TeMoSiAs$_2$/CrI$_3$ heterostructure. In Fig. 8(b), ΔE_σ of TeMoSiAs$_2$/CrI$_3$ is presented as a function of deviation from the equilibrium separation. The black dashed curve is fitted to the following exponential function:

$$\Delta E_\sigma = 4.27e^{-(2.10*\delta)}, \tag{4}$$

where e is the natural constant, and δ represents the interlayer distance deviation from the relaxed state. This analysis clearly demonstrates the high sensitivity of valley splitting to changes in the interlayer distance, following a similar trend observed in WSe$_2$/CrI$_3$ [41]. With a decrease of 0.4 Å in interlayer separation, the valley-splitting energy increases to 9.8 meV, surpassing its equilibrium state by more than 2 times. Conversely, an increase in separation results in diminishing valley polarization, ultimately nearly restoring valley degeneracy with a 2 Å displacement from the equilibrium distance. Additionally, the global band gaps, which indicate the energy difference between the conduction-band edge of CrI$_3$ and the valence-band edge of TeMSiX$_2$, are also adjustable by the interlayer distance. This tunability provides an effective means of separating bands originating from TeMSiX$_2$ and CrI$_3$.

Equations (3) and (4) can be elucidated through the following intuitive description. The magnitude of ΔE_σ is proportional to the magnetic field acting on the TeMoSiAs$_2$ layer. As the magnetization angle of CrI$_3$ changes, the magnetic flux of the TeMoSiAs$_2$ layer can be represented as the surface integral of the normal component of the magnetic field generated by MPE of CrI$_3$, given by

$$\Phi_B = \mathbf{B} \cdot \mathbf{S} = BS\cos\theta. \tag{5}$$

In this equation, **B** represents the magnetic field produced by MPE of CrI$_3$, **S** denotes the unit area of the TeMoSiAs$_2$ layer, and θ signifies the magnetization angle along the z axis, which is equivalent to the angle between the magnetic field and the surface of TeMoSiAs$_2$. Thus the valley polarization varies according to a cosine relationship with θ, as indicated by Eq. (4). Moreover, as the interlayer spacing increases, magnetic coupling decreases exponentially with spacer thickness in insulating systems, as shown in a simple free-electron model [52,53]. Consequently, the strength of the magnetic field generated by MPE on the TeMoSiAs$_2$ layer also decreases exponentially, as indicated by Eq. (4), resulting in a corresponding reduction in the magnitude of ΔE_σ.

IV. SUMMARY

In summary, we identify that TeMSiX$_2$ monolayers present intriguing potential as 2D valleytronic materials. These monolayers, characterized as direct band gap semiconductors, feature two distinct valleys in both the conduction and valence bands. The intrinsic broken inversion symmetry and robust SOC contribute to significant VSS in the valence band, with TeWSiAs$_2$ exhibiting a noteworthy VSS of up to 0.53 eV. This pronounced spin splitting, coupled with the unique valley physics, holds significant promise for realizing valley and spin-Hall effects in TeMSiX$_2$ monolayers. By stacking CrI$_3$ onto TeMSiX$_2$, we induce valley polarization in both band edges. The valley polarization in TeMoSiP$_2$/CrI$_3$ is approximately 2.9 meV, while for TeWSiAs$_2$/CrI$_3$, it can reach as high as 26.1 meV. Furthermore, our study demonstrates that adjustments in magnetization direction and interlayer spacing offer precise control over valley polarization in these heterostructures.

Although there is currently a lack of experimental exploration into valley phenomena, such as the valley Hall effect in Janus materials, the successful development of Janus MoSSe and the existing experimental studies on valley-related properties in MoS$_2$ suggest encouraging prospects for future research in this domain. The structural and electronic resemblances shared by TeMSiX$_2$ monolayers with both MoS$_2$ and WSe$_2$ suggest that these Janus structures may demonstrate analogous valley physics phenomena. By delving into the valley physics of TeMSiX$_2$ monolayers, valuable insights could be gained into their potential applications in emerging technologies such as valleytronics. As such, there is hope for future experiments to explore the valley-related properties of TeMSiX$_2$ monolayers.

[1] G. R. Bhimanapati, Z. Lin, V. Meunier, Y. Jung, J. Cha, S. Das, D. Xiao, Y. Son, M. S. Strano, V. R. Cooper, L. Liang, S. G. Louie, E. Ringe, W. Zhou, S. S. Kim, R. R. Naik, B. G. Sumpter, H. Terrones, F. Xia, Y. Wang *et al.*, ACS Nano **9**, 11509 (2015).

[2] S. Zhang, S. Guo, Z. Chen, Y. Wang, H. Gao, J. GómezHerrero, P. Ares, F. Zamora, Z. Zhu, and H. Zeng, Chem. Soc. Rev. **47**, 982 (2018).

[3] D. Xiao, W. Yao, and Q. Niu, Phys. Rev. Lett. **99**, 236809 (2007).

[4] W. Yao, D. Xiao, and Q. Niu, Phys. Rev. B **77**, 235406 (2008).

[5] D. Xiao, G.-B. Liu, W. Feng, X. Xu, and W. Yao, Phys. Rev. Lett. **108**, 196802 (2012).

[6] K. F. Mak, K. L. McGill, J. Park, and P. L. McEuen, Science **344**, 1489 (2014).

[7] J. R. Schaibley, H. Yu, G. Clark, P. Rivera, J. S. Ross, K. L. Seyler, W. Yao, and X. Xu, Nat. Rev. Mater. **1**, 16055 (2016).

[8] S. A. Vitale, D. Nezich, J. O. Varghese, P. Kim, N. Gedik, P. Jarillo-Herrero, D. Xiao, and M. Rothschild, Small **14**, 1801483 (2018).

[9] G. Pacchioni, Nat. Rev. Mater. **5**, 480 (2020).

[10] W. Choi, N. Choudhary, G. H. Han, J. Park, D. Akinwande, and Y. H. Lee, Mater. Today **20**, 116 (2017).

[11] W. Liao, S. Zhao, F. Li, C. Wang, Y. Ge, H. Wang, S. Wang, and H. Zhang, Nanoscale Horiz. **5**, 787 (2020).

[12] A.-Y. Lu, H. Zhu, J. Xiao, C.-P. Chuu, Y. Han, M.-H. Chiu, C.-C. Cheng, C.-W. Yang, K.-H. Wei, Y. Yang, Y. Wang, D. Sokaras, D. Nordlund, P. Yang, D. A. Muller, M.-Y. Chou, X. Zhang, and L.-J. Li, Nat. Nanotechnol. **12**, 744 (2017).

[13] C. Xia, W. Xiong, J. Du, T. Wang, Y. Peng, and J. Li, Phys. Rev. B **98**, 165424 (2018).

[14] R. Li, Y. Cheng, and W. Huang, Small **14**, 1802091 (2018).

[15] A. Rezavand and N. Ghobadi, J. Magn. Magn. Mater. **544**, 168721 (2022).

[16] R. Peng, Y. Ma, S. Zhang, B. Huang, and Y. Dai, J. Phys. Chem. Lett. **9**, 3612 (2018).

[17] Y.-L. Hong, Z. Liu, L. Wang, T. Zhou, W. Ma, C. Xu, S. Feng, L. Chen, M.-L. Chen, D.-M. Sun, X.-Q. Chen, H.-M. Cheng, and W. Ren, Science **369**, 670 (2020).

[18] S.-D. Guo, W.-Q. Mu, Y.-T. Zhu, R.-Y. Han, and W.-C. Ren, J. Mater. Chem. C **9**, 2464 (2021).

[19] R. Sibatov, R. Meftakhutdinov, and A. Kochaev, Appl. Surf. Sci. **585**, 152465 (2022).

[20] Y. Yu, J. Zhou, Z. Guo, and Z. Sun, ACS Appl. Mater. Interfaces **13**, 28090 (2021).

[21] A. Rezavand and N. Ghobadi, Mater. Sci. Semicond. Process. **152**, 107061 (2022).

[22] G. Kresse and J. Hafner, Phys. Rev. B **47**, 558 (1993).

[23] J. P. Perdew, K. Burke, and M. Ernzerhof, Phys. Rev. Lett. **77**, 3865 (1996).

[24] J. P. Perdew, A. Ruzsinszky, G. I. Csonka, O. A. Vydrov, G. E. Scuseria, L. A. Constantin, X. Zhou, and K. Burke, Phys. Rev. Lett. **100**, 136406 (2008).

[25] J. Heyd, G. E. Scuseria, and M. Ernzerhof, J. Chem. Phys. **118**, 8207 (2003).

[26] See Supplemental Material at http://link.aps.org/supplemental/10.1103/PhysRevB.109.205101 for phonon spectra and AIMD simulations on the stability analysis of TeMSiX_2 monolayers, comprehensive DFT results for TeMSiX_2 monolayers utilizing both GGA and GGA+U approaches, and insights into the properties of other TeMSiX_2/CrI$_3$ heterostructures except TeMoSiP$_2$/CrI$_3$.

[27] A. Togo and I. Tanaka, Scr. Mater. **108**, 1 (2015).

[28] R. N. Barnett and U. Landman, Phys. Rev. B **48**, 2081 (1993).

[29] S. Grimme, J. Antony, S. Ehrlich, and H. Krieg, J. Chem. Phys. **132** (2010).

[30] S. L. Dudarev, G. A. Botton, S. Y. Savrasov, C. J. Humphreys, and A. P. Sutton, Phys. Rev. B **57**, 1505 (1998).

[31] J. L. Lado and J. Fernández-Rossier, 2D Mater. **4**, 035002 (2017).

[32] Y. Yao, L. Kleinman, A. H. MacDonald, J. Sinova, T. Jungwirth, D. S. Wang, E. Wang, and Q. Niu, Phys. Rev. Lett. **92**, 037204 (2004).

[33] C. Ke, Y. Wu, W. Yang, Z. Wu, C. Zhang, X. Li, and J. Kang, Phys. Rev. B **100**, 195435 (2019).

[34] A. A. Mostofi, J. R. Yates, Y.-S. Lee, I. Souza, D. Vanderbilt, and N. Marzari, Comput. Phys. Commun. **178**, 685 (2008).

[35] A. A. Mostofi, J. R. Yates, G. Pizzi, Y.-S. Lee, I. Souza, D. Vanderbilt, and N. Marzari, Comput. Phys. Commun. **185**, 2309 (2014).

[36] K. F. Mak, C. Lee, J. Hone, J. Shan, and T. F. Heinz, Phys. Rev. Lett. **105**, 136805 (2010).

[37] A. Splendiani, L. Sun, Y. Zhang, T. Li, J. Kim, C.-Y. Chim, G. Galli, and F. Wang, Nano Lett. **10**, 1271 (2010).

[38] D. C. Elias, R. R. Nair, T. M. G. Mohiuddin, S. V. Morozov, P. Blake, M. P. Halsall, A. C. Ferrari, D. W. Boukhvalov, M. I. Katsnelson, A. K. Geim, and K. S. Novoselov, Science **323**, 610 (2009).

[39] D. Zhong, K. L. Seyler, X. Linpeng, R. Cheng, N. Sivadas, B. Huang, E. Schmidgall, T. Taniguchi, K. Watanabe, M. A. McGuire, W. Yao, D. Xiao, K.-M. C. Fu, and X. Xu, Sci. Adv. **3**, e1603113 (2017).

[40] K. L. Seyler, D. Zhong, B. Huang, X. Linpeng, N. P. Wilson, T. Taniguchi, K. Watanabe, W. Yao, D. Xiao, M. A. McGuire, K.-M. C. Fu, and X. Xu, Nano Lett. **18**, 3823 (2018).

[41] T. Hu, G. Zhao, H. Gao, Y. Wu, J. Hong, A. Stroppa, and W. Ren, Phys. Rev. B **101**, 125401 (2020).

[42] Z. Zhang, X. Ni, H. Huang, L. Hu, and F. Liu, Phys. Rev. B **99**, 115441 (2019).

[43] J. Zhao, X. Jin, H. Zeng, C. Yao, and G. Yan, Appl. Phys. Lett. **119**, 213101 (2021).

[44] H. Zeng, R.-S. Chen, and G. Yao, Adv. Electron. Mater. **6**, 1901024 (2020).

[45] M. A. McGuire, H. Dixit, V. R. Cooper, and B. C. Sales, Chem. Mater. **27**, 612 (2015).

[46] W.-B. Zhang, Q. Qu, P. Zhu, and C.-H. Lam, J. Mater. Chem. C **3**, 12457 (2015).

[47] A. Srivastava, M. Sidler, A. V. Allain, D. S. Lembke, A. Kis, and A. İmamoğlu, Nat. Phys. **11**, 141 (2015).

[48] D. MacNeill, C. Heikes, K. F. Mak, Z. Anderson, A. Kormányos, V. Zólyomi, J. Park, and D. C. Ralph, Phys. Rev. Lett. **114**, 037401 (2015).

[49] Y. Li, J. Ludwig, T. Low, A. Chernikov, X. Cui, G. Arefe, Y. D. Kim, A. M. van der Zande, A. Rigosi, H. M. Hill, S. H. Kim, J.

Hone, Z. Li, D. Smirnov, and T. F. Heinz, Phys. Rev. Lett. **113**, 266804 (2014).

[50] A. V. Stier, K. M. McCreary, B. T. Jonker, J. Kono, and S. A. Crooker, Nat. Commun. **7**, 10643 (2016).

[51] Y. J. Wu, C. Shen, Q. H. Tan, J. Shi, X. F. Liu, Z. H. Wu, J. Zhang, P. H. Tan, and H. Z. Zheng, Appl. Phys. Lett. **112**, 153105 (2018).

[52] J. C. Slonczewski, Phys. Rev. B **39**, 6995 (1989).

[53] P. Bruno, Phys. Rev. B **49**, 13231 (1994).